Aeroelastic Analysis of T-Tails Using an Enhanced Doublet Lattice Method

Louw H. van Zyl* and Edward H. Mathews†

North-West University, Pretoria 0040, South Africa

The subsonic doublet lattice method is widely used to calculate unsteady air loads for aeroelastic analyses. Despite its widespread use and significant improvements in other aspects of the method, its application to the flutter analysis of T-tail aircraft is lagging in terms of accuracy and the efficiency of the process. In particular, the doublet lattice method does not calculate all the necessary aerodynamic loads for T-tail flutter analysis. It is common practice to calculate additional aerodynamic loads outside of the doublet lattice method and add them to the doublet lattice method results before solving the flutter equation. This paper describes the extension of the doublet lattice method to account for these loads. The boundary condition is made more general to account for yaw/dihedral and sideslip/dihedral coupling. The calculation of forces is generalized to account for lateral load due to roll and roll rate, rolling moment due to yaw, yaw rate and oscillatory sideslip, and yawing moment due to roll rate. In addition, the steady-state load and the quadratic mode shapes are taken into account in the calculation of generalized forces.

Nomenclature

C_p = pressure coefficient, $C_p^0 + C_p^1 e^{i\omega t}$
C_p^0 = steady pressure coefficient
C_p^1 = unsteady pressure coefficient
$\mathbf{F}$ = total force vector, $\mathbf{F}_0 + \mathbf{F}_1 e^{i\omega t}$
$\mathbf{F}_j$ = unsteady force vector due to mode j
$\mathbf{F}_0$ = steady-state force vector
$\mathbf{F}_1$ = total unsteady force vector, $\sum_{j=1}^{n} q_j \mathbf{F}_j$
$\mathbf{h}$ = displacement vector
$\mathbf{h}_i^{(1)}$ = linear modal displacement due to mode i
$\mathbf{h}_{ij}^{(2)}$ = quadratic modal displacement due to modes i and j
k = reduced frequency
$\mathbf{n}$ = instantaneous normal vector, $\mathbf{n}_0 + \mathbf{r} e^{i\omega t} \times \mathbf{n}_0$
$\mathbf{n}_0$ = mean normal vector
$\{Q\}$ = vector of generalized forces, $[Q]\{q\}$
$[Q]$ = aerodynamic matrix relating generalized coordinates to generalized forces
$\{q\}$ = vector of generalized coordinates
Q_i = generalized force i
q_j = generalized coordinate j
$\mathbf{r}$ = rotation vector
U = freestream velocity magnitude
$\mathbf{u}$ = normalized instantaneous total velocity vector, $\mathbf{u}_\infty + \mathbf{u}_0 + \mathbf{u}_1 e^{i\omega t}$
$\mathbf{u}_0$ = normalized steady perturbation velocity vector
$\mathbf{u}_1$ = normalized unsteady perturbation velocity vector
$\mathbf{u}_\infty$ = normalized freestream velocity vector
Γ = normalized total circulation vector, $\Gamma_0 + \Gamma_1 e^{i\omega t} + \mathbf{r} e^{i\omega t} \times \Gamma_0$
Γ_0 = normalized steady circulation vector
Γ_1 = normalized unsteady circulation vector
ω = angular frequency
ω_r = wave number, $i\omega/U$

*Ph.D. Candidate, Centre for Research and Continued Engineering Development, Suite 90, Private Bag X30; lvzyl@csir.co.za.

†Professor, Centre for Research and Continued Engineering Development, Suite 90, Private Bag X30; ehmathews@researchtoolbox.com.

Introduction

THE subsonic doublet lattice method (DLM) [1–5] has been the workhorse of aeroelastic analysis for several decades. Despite its widespread use, the popular implementations of the DLM are not suitable for the analysis of T-tail flutter. The essence of the T-tail problem is that the DLM only calculates the unsteady aerodynamic loads and generalized forces due to pitching and plunging of a lifting surface. This is acceptable for a conventional horizontal tail plane (HTP); however, in the case of a T-tail, the HTP is positioned on top of a flexible fin. The HTP is therefore subjected to significant rolling, yawing, and spanwise in-plane motion (i.e., motion in the plane of the HTP), in addition to the usual pitching and plunging motions. Both in-plane loads and normal loads due to in-plane motion become important.

In addition to including in-plane motions and loads in the analysis, it is also necessary to consider the quadratic component of the natural modes. For example, in the case of a fin bending mode, the top of the fin moves along a circular arc. In the case of a fin torsion mode, the fin actually shortens and the HTP moves normal to itself. Under these conditions, the steady-state load on the HTP contributes significantly to the unsteady generalized forces.

A further complication is that the incremental aerodynamic loads due to roll and yaw acting on the HTP are dependent on the steady-state aerodynamic load. In practical terms, this complication adds another dimension to the flight envelope that needs to be cleared for flutter; that is, in addition to altitude, speed, and aircraft configuration, the range in steady-state loading on the HTP needs to be considered.

The T-tail extensions were implemented in the wing–body DLM of [6]. This code employs a more general boundary condition than the DLM of [2–5] that accounts for yaw/dihedral and sideslip/dihedral coupling. The same code is used to solve the steady flowfield and the unsteady loads. In the present study, the calculation of unsteady forces were generalized to account for the in-plane loads, as well as the normal loads due to in-plane motions. In addition, the steady-state load and the quadratic mode shape components were taken into account in the calculation of generalized forces.

Theory

The DLM of [2–5] solves for the unsteady pressure distribution over lifting surfaces by satisfying the unsteady boundary condition at a number of points on the surface. Although this method uses the downwash formula of a horseshoe vortex in the calculation of the unsteady downwash of an acceleration potential doublet line, the steady pressure distribution is not solved for, and there is no

superposition of the steady and unsteady flowfields. In the wing–body DLM of [6], the steady flowfield is solved using a vortex lattice method before the unsteady flowfield is solved using a DLM. The unsteady boundary condition is not affected by the steady flowfield. The steady flowfield influences the unsteady loads only through the nonlinear expression used to calculate the pressures on body surface panels.

In the case of T-tails, the steady loading on the HTP contributes significantly to the unsteady loads through the change in orientation of the steady vortex filaments, as well as the oscillatory velocity of the steady vortex filaments due to the vibration of the structure. The solution process of the enhanced DLM is identical to that of the wing–body DLM described in [6] up to the point of calculating the unsteady pressure distribution. The unsteady pressure distribution is then used to generate a quasi-steady vortex distribution, which is added to the steady vortex distribution before the forces are calculated using the Kutta–Joukowski law. In the absence of any steady loading, this method produces identical results to the standard DLM.

In the following sections, the boundary condition is briefly stated, and then the calculation of forces is addressed. The calculation of in-plane loads and of normal loads due to in-plane motion is based on the work of Queijo [7]. In essence, the procedure that Queijo applied to a lifting line distribution is applied at the aerodynamic box level in the DLM.

Boundary Condition

The same boundary condition is used for body panels and for lifting surface panels. The general form of the boundary condition is (see Fig. 1)

$$\dot{\mathbf{h}} \cdot \mathbf{n} = \mathbf{u} \cdot \mathbf{n} \tag{1}$$

or

$$\begin{aligned}
\omega_r \mathbf{h} e^{i\omega t} \cdot (\mathbf{n}_0 + \mathbf{r} e^{i\omega t} \times \mathbf{n}_0) \\
= (\mathbf{u}_\infty + \mathbf{u}_0 + \mathbf{u}_1 e^{i\omega t} + \mathbf{h} \cdot \nabla \mathbf{u}) \cdot (\mathbf{n}_0 + \mathbf{r} e^{i\omega t} \times \mathbf{n}_0)
\end{aligned} \tag{2}$$

The steady boundary condition is simply

$$\mathbf{u}_0 \cdot \mathbf{n}_0 = -\mathbf{u}_\infty \cdot \mathbf{n}_0 \tag{3}$$

For reasons given in [6], the term $\mathbf{h} \cdot \nabla \mathbf{u}$ is ignored. Based on this assumption, the unsteady boundary condition is given by

$$\mathbf{u}_1 \cdot \mathbf{n}_0 = \omega_r \mathbf{h} \cdot \mathbf{n}_0 - \mathbf{u}_\infty \cdot (\mathbf{r} \times \mathbf{n}_0) \tag{4}$$

The general form of the second factor in the second term takes account of yaw/dihedral coupling, and the general form of the first term takes account of unsteady sideslip/dihedral coupling (note that $\omega_r \mathbf{h}$ may represent the unsteady sideslip velocity).
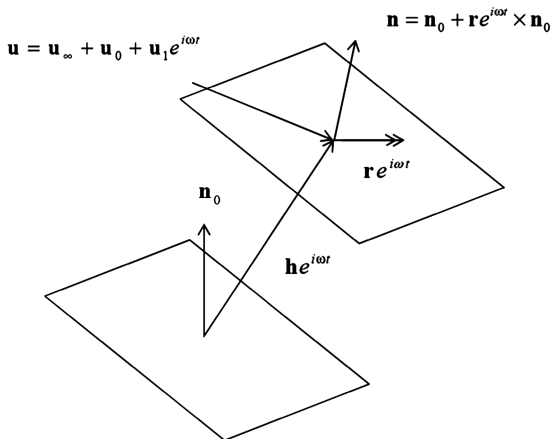
Forces on Lifting Surface Panels

The downwash equation of the DLM is usually cast in a form that relates a pressure differential over a panel to induced velocity. However, the underlying mathematical model actually relates the strength of an acceleration potential doublet line, located at the box quarter-chord, to induced velocity. It is convenient for T-tail configurations to calculate the forces on lifting surface boxes using the Kutta–Joukowski law, i.e., as the cross product of the flow velocity and the circulation vector (see Fig. 2):

$$\mathbf{F} = \mathbf{V} \times \Gamma \tag{5}$$

where $\mathbf{F}$ is the force normalized by dynamic pressure, and $\mathbf{V}$ is the relative flow velocity normalized by the freestream velocity. The quarter-chord circulation vector Γ is minus one-half the box chord times the pressure coefficient differential (as determined by solving the downwash equation) multiplied by the vector from the doublet line inboard end to the outboard end.

Three vortex elements per box need to be considered: the quarter-chord bound vortex and the two chordwise-bound trailing vortices. The strength of the quarter-chord bound vortex is derived from the box pressure differential. The strength of the chordwise-bound vortices is given by the sum of the strengths of the upstream quarter-chord bound vortices. The total circulation of any of these vortex elements can be expressed as

$$\Gamma = \Gamma_0 + \Gamma_1 e^{i\omega t} + \mathbf{r} e^{i\omega t} \times \Gamma_0 \tag{6}$$

The total relative velocity is given by

$$\mathbf{V} = \mathbf{u}_\infty + \mathbf{u}_0 + \mathbf{u}_1 e^{i\omega t} - \omega_r \mathbf{h} e^{i\omega t} \tag{7}$$

The induced velocity and modal displacement are those at the doublet line midpoint. The steady part of the total force is given by

$$\mathbf{F}_0 = (\mathbf{u}_\infty + \mathbf{u}_0) \times \Gamma_0 \tag{8}$$

The first harmonic of the total force is given by

$$\begin{aligned}
\mathbf{F}_1 = (\mathbf{u}_\infty + \mathbf{u}_0) \times \Gamma_1 + (\mathbf{u}_\infty + \mathbf{u}_0) \times (\mathbf{r} \times \Gamma_0) \\
+ (\mathbf{u}_1 - \omega_r \mathbf{h}) \times \Gamma_0
\end{aligned} \tag{9}$$

The first term includes the normal force that is usually calculated by the DLM and is due to the unsteady circulation. The term $\mathbf{u}_0$ is usually neglected, as it is small compared with $\mathbf{u}_\infty$.

The second term is due to the change in direction of the steady circulation vector. This accounts for both lateral load due to roll and rolling moment due to yaw (in the case of a swept HTP). The lateral load due to roll was included by Jennings and Berry [8], as well as Suciu [9]. However, it will be shown that this force should not be considered in isolation from the quadratic mode shape components.

The third term includes the unsteady induced drag and the unsteady lift and drag due to the motion of the doublet line. This way of calculating induced drag is not physically correct but fortuitously provides a useful estimate [10–12].

The calculation of the forces resulting from the interaction of spanwise flow with the chordwise-bound vortices needs further consideration. In the vortex lattice method, the trailing vortices
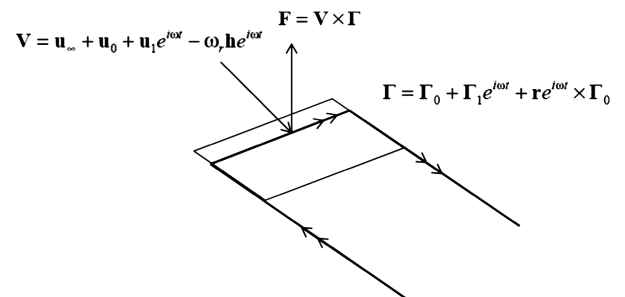

Fig. 1   Vectors for calculating the boundary condition of a source panel.

Fig. 2   Vectors for calculating forces on a lifting surface panel.

(i.e., the chordwise-bound vortices) have constant strength from one bound vortex to the next downstream bound vortex, or to the wing trailing edge. In the present method, these segments of the chordwise-bound vortices are associated with the upstream aerodynamic box. The displacements of the vortex segment midpoints are calculated from the upstream box modal displacements, and the flow velocities at these points are taken to be the same as at the bound vortex midpoint, except that the normal component is removed. In the case of an isolated flat wing, the wing elements do not induce in-plane velocities in the plane of the wing. The gradients of the in-plane velocities are therefore small, and it is justified not to compute induced velocities at each trailing vortex segment midpoint.

In unsteady flow, the strength of the trailing vortices also varies in the chordwise direction due to the flow unsteadiness. This spatial variation is accompanied by a continuous sheet of vorticity being shed from the doublet line. This sheet of shed vorticity is, however, convected downstream by the flow, and no force is generated from it.

Forces on Body Panels

In the case of body surface panels, the force is calculated as the product of the instantaneous pressure and the instantaneous normal vector. The force is given by

$$\mathbf{F} = -C_p \mathbf{n} \tag{10}$$

Note that the normal vector is not a unit vector, but it has a length equal to the panel area, and note that the normal vector has a steady and an unsteady component. The pressure coefficient is given by

$$C_p = C_p^0 + e^{i\omega t} C_p^1 \tag{11}$$

and the instantaneous normal vector is given by

$$\mathbf{n} = \mathbf{n}_0 + \mathbf{r} e^{i\omega t} \times \mathbf{n}_0 \tag{12}$$

The steady part of the force is

$$\mathbf{F}_0 = -C_p^0 \mathbf{n}_0 \tag{13}$$

and the first harmonic is

$$\mathbf{F}_1 = -C_p^0 (\mathbf{r} \times \mathbf{n}_0) - C_p^1 \mathbf{n}_0 \tag{14}$$

The first term is the unsteady component due to the rotation of the steady force vector, and the second term is due to the unsteady pressure on the panel. All the modal displacements and rotations are those at the panel centroid.

Generalized Forces

The forces calculated as described previously (in particular, the unsteady force due to the rotation of a steady force vector) may lead to spurious generalized forces if a linear description of the modal displacement is used. Quadratic mode shapes were first proposed by Dohrmann and Segalman [13] and are routinely used in the analysis of beamlike structures in rotating systems, such as helicopter rotor blades and even robotics [14]. It has also been applied to slender wings with large steady-state deflections, such as the high-altitude long-endurance class of unmanned air vehicles [15]. The present study indicates that quadratic mode shapes should also be used in the flutter analysis of T-tails.

Assuming a parabolic modal displacement model, the displacement of the doublet line midpoint of a lifting surface panel, or the centroid of a body surface panel, can be expressed as (cf. Eq. 3 of [13])

$$\mathbf{h} = \sum_{i=1}^{n} q_i \mathbf{h}_i^{(1)} + \sum_{i=1}^{n} \sum_{k=1}^{n} q_i q_k \mathbf{h}_{ik}^{(2)} \tag{15}$$

Making use of the symmetry of quadratic mode shapes [i.e., $\mathbf{h}_{ik}^{(2)} = \mathbf{h}_{ki}^{(2)}$], the virtual displacement is given by

$$\delta \mathbf{h} = \sum_{i=1}^{n} \delta q_i \mathbf{h}_i^{(1)} + \sum_{i=1}^{n} \sum_{k=1}^{n} (\delta q_i q_k + q_i \delta q_k) \mathbf{h}_{ik}^{(2)}$$

$$= \sum_{i=1}^{n} \delta q_i \mathbf{h}_i^{(1)} + 2 \sum_{i=1}^{n} \sum_{k=1}^{n} \delta q_i q_k \mathbf{h}_{ik}^{(2)} \tag{16}$$

The total force on a panel is given by the sum of the steady-state force and the unsteady force due to each mode:

$$\mathbf{F} = \mathbf{F}_0 + \sum_{j=1}^{n} q_j \mathbf{F}_j \tag{17}$$

Virtual work is defined in terms of the generalized forces as

$$\delta W = \sum_{i=1}^{n} \delta q_i Q_i = \sum_{i=1}^{n} \delta q_i \sum_{j=1}^{n} Q_{ij} q_j \tag{18}$$

The virtual work can also be derived from Eqs. (16) and (17) to be

$$\delta W = \delta \mathbf{h} \cdot \mathbf{F} = \sum_{i=1}^{n} \delta q_i \mathbf{h}_i^{(1)} \cdot \left(\mathbf{F}_0 + \sum_{j=1}^{n} q_j \mathbf{F}_j \right)$$

$$+ 2 \sum_{i=1}^{n} \sum_{k=1}^{n} \delta q_i q_k \mathbf{h}_{ik}^{(2)} \cdot \left(\mathbf{F}_0 + \sum_{j=1}^{n} q_j \mathbf{F}_j \right)$$

$$= \sum_{i=1}^{n} \delta q_i \mathbf{h}_i^{(1)} \cdot \mathbf{F}_0 + 2 \sum_{i=1}^{n} \sum_{k=1}^{n} \delta q_i q_k \mathbf{h}_{ik}^{(2)} \cdot \mathbf{F}_0$$

$$+ \sum_{i=1}^{n} \sum_{j=1}^{n} \delta q_i q_j \mathbf{h}_i^{(1)} \cdot \mathbf{F}_j + 2 \sum_{i=1}^{n} \sum_{k=1}^{n} \sum_{j=1}^{n} \delta q_i q_k q_j \mathbf{h}_{ik}^{(2)} \cdot \mathbf{F}_j \tag{19}$$

Comparing Eqs. (18) and (19) and considering only terms that are linear in q, the generalized forces can be extracted as

$$Q_i = \sum_{j=1}^{n} q_j \mathbf{h}_i^{(1)} \cdot \mathbf{F}_j + 2 \sum_{k=1}^{n} q_k \mathbf{h}_{ik}^{(2)} \cdot \mathbf{F}_0 \tag{20}$$

The elements of the generalized force matrix are therefore defined by

$$Q_{ij} = \mathbf{h}_i^{(1)} \cdot \mathbf{F}_j + 2 \mathbf{h}_{ij}^{(2)} \cdot \mathbf{F}_0 \tag{21}$$

A complete parabolic modal displacement model for n modes would involve n^2 quadratic modes [of which only $n(n + 1)/2$ would be unique due to symmetry of the quadratic mode shape components]. This would amount to a prohibitive amount of quadratic modes, even for a light aircraft. In many cases, it may be sufficient to consider only the quadratic components of individual modes. The quadratic mode shapes are coupled through the modal rotations; therefore, the fin bending and torsion modes are not strongly coupled: for the fin bending mode, the modal rotation vector of any part of the empennage is approximately normal to the fin elastic axis, whereas for the fin torsion mode, the modal rotation vector of any part of the empennage is approximately parallel to the fin elastic axis.

Case for Parabolic Mode Shapes

The application of parabolic mode shapes to the flutter analysis of T-tails is believed to be novel; therefore, an example illustrating its application to a simple problem seems in order. This example could be solved by simple logic or kinematics but not using Lagrange's equation and linear mode shapes. Lagrange's equation, retaining only the terms relevant to fixed-wing aircraft, states

$$\frac{\mathrm{d}}{\mathrm{d}t} \left(\frac{\mathrm{d}T}{\mathrm{d}\dot{q}_i} \right) + \frac{\mathrm{d}U}{\mathrm{d}q_i} = Q_i \tag{22}$$

where T is the kinetic energy of the system, U is the potential energy of the system, q_i are the degrees of freedom, and Q_i are the

generalized forces. The flutter equation is derived from Lagrange's equation and states

$$[M]\{\ddot{q}\} + [C]\{\dot{q}\} + [K]\{q\} = \{Q\} \qquad (23)$$

where $[M]$ is the mass matrix, $[C]$ is the damping matrix, $[K]$ is the stiffness matrix, $\{q\}$ is the vector of generalized coordinates (i.e., degrees of freedom), and $\{Q\}$ is the vector of generalized forces.

The steady-state trim load on the HTP of a T-tail introduces effects that are not usually accounted for in a flutter analysis, including aerodynamic coupling terms such as rolling moment due to yaw rate and stiffness effect. Only the latter is discussed here.

The T-tail of this example has one degree of freedom (viz., roll about the root of the fin) denoted by ϕ. In keeping with the convention of [9], roll to the left is taken as positive. The fin height is h, and the lateral and vertical displacements at the top of the fin are y and z, respectively (see Fig. 3). The exact path and the parabolic approximation to the exact path of the top of the fin are given by

$$y = -h \sin \phi \approx -h\phi \qquad z = -h(1 - \cos \phi) \approx -\tfrac{1}{2}h\phi^2 \qquad (24)$$

The aerodynamic load is an upward force L_0 that always acts normal to and in the center of the HTP (Fig. 3). Assuming a mass moment of inertia of I about the roll axis and a torsional spring stiffness of K_T, the kinetic and potential energy of the system can be expressed as

$$T = \tfrac{1}{2}I\dot{\phi}^2 \qquad U = \tfrac{1}{2}K_T\phi^2 \qquad (25)$$

The side force due to the roll of the HTP, according to both Jennings and Berry [8] and Suciu [9], is given by

$$L_y = -L_0\phi \qquad (26)$$

Where L_y is the unsteady side force, positive to the right (for the purpose of this example, we regard the HTP as a single strip). Assuming a linear mode shape [i.e., discarding the quadratic term in Eq. (24)], the displacement and virtual displacement of the top of the fin, the application point of the aerodynamic load, are given by

$$\mathbf{h} = (0, -h\varphi, 0) \qquad \delta\mathbf{h} = (0, -h, 0)\delta\varphi \qquad (27)$$

The virtual work is given by the product of the generalized force and the variation in the generalized coordinate, and it is given by the product of the actual force and the virtual displacement:

$$\delta W = Q\delta\varphi = \mathbf{F} \cdot \delta\mathbf{h} = (0, -L_0\varphi, L_0) \cdot (0, -h, 0)\delta\varphi = L_0 h\varphi\delta\varphi \qquad (28)$$

from which the generalized force can be derived to be $Q = L_0 h\varphi$. Substituting this expression for the generalized force and the

$$y \approx -h\phi$$
$$\delta y = -h\delta\phi$$
$$z \approx -\tfrac{1}{2}h\phi^2$$
$$\delta z = -h\phi\delta\phi$$
$$\delta W = L_y \delta y + L_z \delta z$$
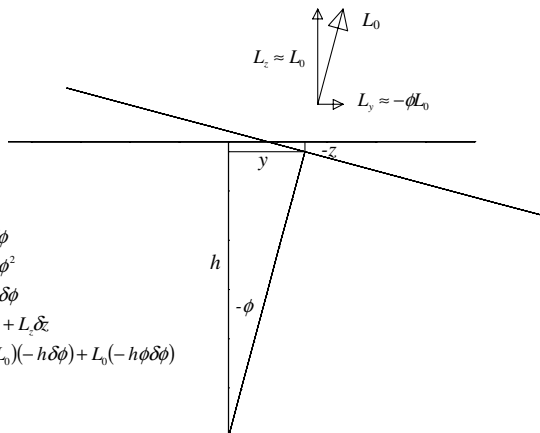$$= (-\phi L_0)(-h\delta\phi) + L_0(-h\phi\delta\phi)$$
$$= 0$$

Fig. 3 Cancellation of virtual work terms for a T-tail hinging about the root of the fin.

expressions for kinetic and potential energy in Eq. (25) into Lagrange's equation, Eq. (22) yields

$$I\ddot{\phi} + (K_T - L_0 h)\phi = 0 \qquad (29)$$

Thus, the side force due to rolling of the HTP resulted in a stiffness term in the flutter equation. This term is totally spurious, since the force always acts through the rotation axis and can have no stiffness contribution. The origin of this spurious stiffness term lies in the virtual displacement [Eq. (27)]. According to the linear displacement model, the direction of motion remains horizontal, while in reality, the direction of motion changes to remain normal to the force L_0. The effect of this spurious term is that an upward trim load would erroneously decrease the stiffness of the fin bending mode (decreasing the divergence speed, if applicable) and vice versa.

The exact circular or approximate parabolic path of the top of the fin, on the other hand, is always normal to the direction of the load. If a parabolic mode shape description was used, Eq. (27) would read

$$\mathbf{h} = (0, -h\varphi, -\tfrac{1}{2}h\varphi^2) \qquad \delta\mathbf{h} = (0, -h, -h\varphi)\delta\varphi \qquad (30)$$

The virtual work would be zero, given by

$$\delta W = \mathbf{F} \cdot \delta\mathbf{h} = (0, -L_0\varphi, L_0) \cdot (0, -h, -h\varphi)\delta y = 0 \qquad (31)$$

Thus, the spurious stiffness term would be removed. In this example, it would have been more accurate to ignore the side force due to roll, as well as the quadratic modal displacement, than to include only the side force due to roll. In practice, where the fin bends rather than hinges about its root, these two contributions seldom cancel completely, and the only accurate option is to include both.

Calculated Results

Results from the present DLM were compared with Queijo's results [7] for isolated wings executing rigid body motions. The present method was also applied to Stark's T-tail [16], which has no dihedral and no static load, and to the flutter analysis of a T-tail flutter model.

Comparison with Queijo's Results for Isolated Wings

Both Jennings and Berry [8] and Suciu [9] used Queijo's method [7] to obtain the additional aerodynamic forces for T-tail flutter analysis. It is therefore important to show that the present enhanced DLM produces similar results for isolated wings. Queijo gave extensive results for the following parameters for isolated wings without dihedral: 1) C_{l_β}/C_L rolling moment due to sideslip, 2) C_{l_r}/C_L rolling moment due to yaw rate, 3) C_{l_p} roll damping, 4) C_{Y_p}/C_L side force due to roll rate, and 5) C_{n_p}/C_L yawing moment due to roll rate.

Note that, of all these parameters, the popular implementations of the DLM would only calculate roll damping. For the rest of the parameters, it would effectively return a zero. Both Jennings and Berry [8] and Suciu [9] accounted for rolling moment due to yaw rate but not for yawing moment due to roll rate. Rodden [17] pointed out that the two terms are of the same magnitude. Both terms are accounted for in the enhanced DLM.

In the enhanced DLM code, it is possible to specify the steady-state angle of attack, the steady-state angle of sideslip and the six rigid body degrees of freedom as modes. The six degrees of freedom are 1) x displacement, 2) z displacement, 3) pitch, 4) y displacement, 5) yaw, and 6) roll.

The pitch and yaw rotations are specified around the origin, i.e., the root quarter-chord point. For some of Queijo's results [7], the rotation center is specified as the aerodynamic center. It is therefore necessary to determine the aerodynamic center from

$$x_{ac} = -\frac{Q_{30}}{Q_{20}} \qquad (32)$$

where Q_{ij} is the generalized force corresponding to pressure mode j and displacement mode i. If j is zero, it indicates the steady-state (or mean) pressure distribution.

The estimates for Queijo's parameters [7] in terms of the generalized forces calculated by the present method are given by

$$\frac{C_{l_\beta}}{C_L} = -\frac{Q_{60}/\beta}{bQ_{20}} = -\frac{\mathrm{Re}(Q_{65})}{bQ_{20}}\bigg|_{k=0} = -\frac{\mathrm{Im}(Q_{64})/|\omega_r|}{bQ_{20}}\bigg|_{k=0.01} \quad (33)$$

$$\frac{C_{l_r}}{C_L} = \frac{[\mathrm{Im}(Q_{65}) - x_{\mathrm{ac}}\mathrm{Im}(Q_{64})]/|\omega_r|}{(b^2/2)Q_{20}} \quad (34)$$

$$C_{l_p} = \frac{\mathrm{Im}(Q_{66})/|\omega_r|}{Sb^2/2} \quad (35)$$

$$\frac{C_{Y_p}}{C_L} = -\frac{\mathrm{Im}(Q_{46})/|\omega_r|}{(b/2)Q_{20}} \quad (36)$$

$$\frac{C_{n_p}}{C_L} = \frac{[\mathrm{Im}(Q_{56}) - x_{\mathrm{ac}}\mathrm{Im}(Q_{46})]/|\omega_r|}{(b^2/2)Q_{20}} \quad (37)$$

The results presented in Fig. 4 are for a family of wing planforms with a taper ratio of 0.5 and different sweep angles and aspect ratios. Each line on the graph corresponds to a constant sweep angle (indicated in the legend) and varying aspect ratio (the abscissa). Queijo's results [7], shown in Fig. 4, were obtained by digitizing his plots of $\bar{y}^*$ and $\tilde{y}^*$ and using the dig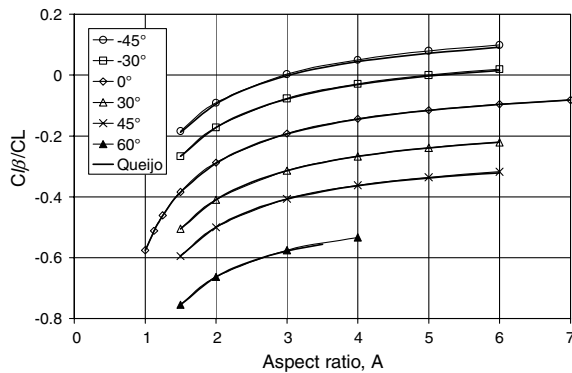itized values in his expressions for the relevant parameters. Sixty-four spanwise strips on each semispan were used in the present method.

The parameters rolling moment due to sideslip (see Fig. 4a) and rolling moment due to yaw rate (see Fig. 4b) compared well, except for the correction of 0.05 added to the rolling moment due to sideslip parameter by Queijo [7]. In the comparison in Fig. 4, this correction was omitted from Queijo's results.
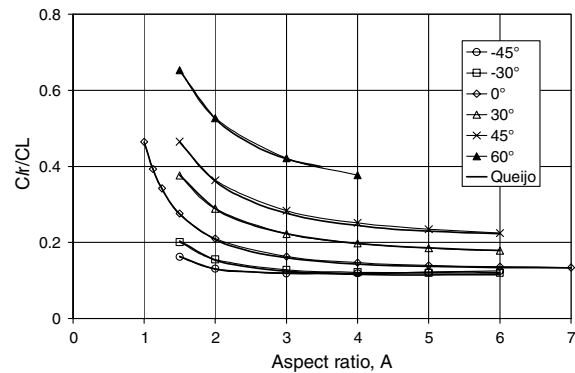
The other parameters depend on the circulation distribution due to roll rate, for which Queijo used a crude approximation [7]. The initial comparison between the present results and Queijo's was therefore not satisfactory. Queijo's approximation could, however, easily be incorporated into the present method in order to make a meaningful comparison. The load distribution due to angle of attack was first calculated using the present method. Queijo's equation [Eq. (4)] was then used to derive the circulation distribution due to roll rate. With this approximation incorporated in the present DLM, the results for roll damping compared favorably. The present DLM calculation of roll damping is identical to that of the standard DLM, and the results are not presented here.

The results for side force due to roll rate still did not compare well, even with this approximation for the roll-induced load distribution. The side force and yawing moment due to roll rate result from the interaction of the roll velocity and the steady-state (angle of attack) circulation. The present method uses the relative velocity of the air flow (which is the resultant of the wing motion, the freestream, and the induced velocity at the doublet line midpoint) to determine the load on the doublet line, whereas Queijo [7] neglected the induced velocity. In the comparison shown in Figs. 4c and 4d, the induced velocity was also ignored in the present method.
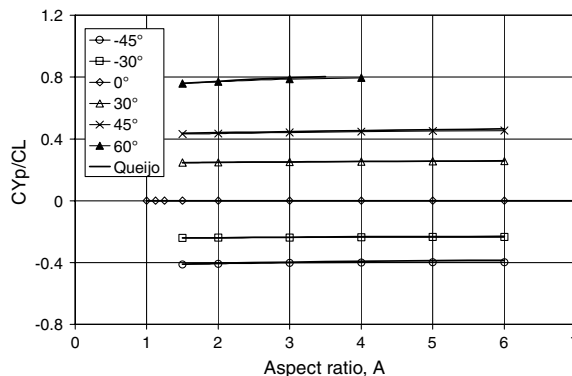
The seemingly good comparison in Fig. 4 does not prove that the present DLM is equivalent to Queijo's method [7] but, rather, that all the differences between the methods can be accounted for. The issue of induced velocity in the calculation of side force and yawing moment due to roll rate needs to be investigated further.
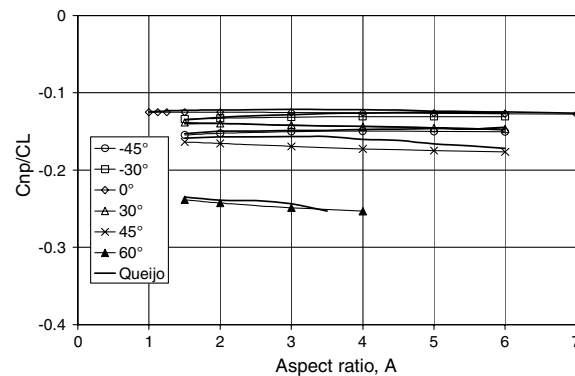
a)

b)

c)

d)

Fig. 4   Comparison of present method with Queijo's results [7] for isolated wings: a) rolling moment due to sideslip, b) rolling moment due to yaw rate, c) side force due to roll rate, and d) yawing moment due to roll rate.
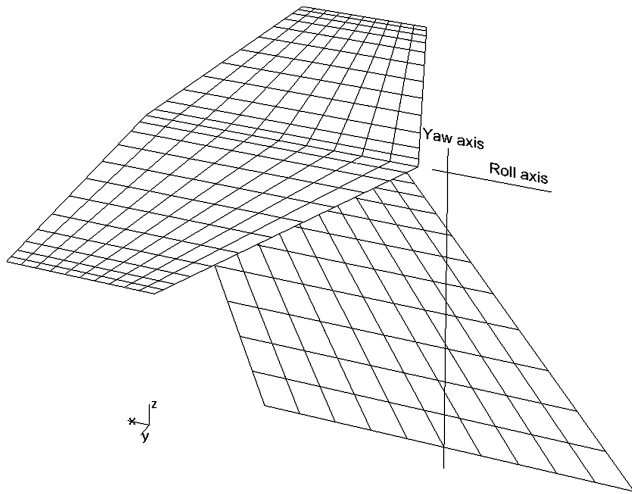
Fig. 5   Aerodynamic model of Stark's T-tail [16].

Generalized Forces for a T-Tail Without Dihedral or Steady Loads

Kalman et al. [18] presented static and unsteady generalized forces for Stark's T-tail [16] around zero sideslip and angle of attack, calculated using a DLM. The enhanced DLM should produce the same results as the original DLM in the absence of a dihedral or a steady load. This was verified by repeating the analysis of [18] using the enhanced DLM. The aerodynamic model used in the present study is shown in Fig. 5. The results of the enhanced DLM are compared with the results of [18], in Tables 1 and 2, for the static and unsteady generalized forces, respectively. Stark's original results [16], as well as the more recent unsteady results of Dusto and Epton [19] from a panel method that uses distributed source and doublet panels, are also shown. The enhanced DLM and the DLM of [6] produced identical results for this case.

The reference length in the definition of the reduced frequency is equal to one-third of the stabilizer semispan, and the generalized aerodynamic forces are defined by

$$Q_{ij} = \frac{1}{4\pi b} \iint h_i p_j \, ds \qquad (38)$$

Where b is the stabilizer semispan; h_i for $i = 1, 2, 3$ describes the surface normal displacement for unit yaw, sideslip, and roll; and p_j for $j = 1, 2, 3$ describes the complex pressure coefficient distribution induced by the same set of displacements. The paneling scheme used in [18] was not reported, and the DLM of [18] did not employ the same kernel approximation or spanwise integration scheme as the present method. The results can therefore not be expected to be identical but are generally in good agreement.

Flutter Analysis and Wind-Tunnel Testing of T-Tail Flutter Model

A T-tail flutter model with sweptback fin and stabilizers was constructed from steel and aluminium, covered with balsa wood and plastic film. The fin of the model was not tapered, it had a height of 0.497 m and a chord of 0.425 m, and it was swept back by 33.1 deg. An unswept and untapered fin tip fairing with a height of 0.098 m and a chord of 0.528 m was mounted on top of the fin so that the fin and fin tip fairing leading edges joined up. The stabilizers, which had no dihedral, were mounted at midheight of the fin tip fairing. The stabilizers had a root chord of 0.363 m, a semispan of 0.625 m, a taper ratio of 0.276, and a leading-edge sweep angle of 36.5 deg. The pitch axis of the stabilizers passed through 74.1% root chord, which coincided with 60.6% of the fin tip fairing chord. The stabilizers had a NACA 23015 airfoil section and could be mounted upright or upside down. The purpose of the cambered profile was to enable larger trim loads on the HTP to be achieved without stalling.

The model had a roll hinge and spring at the root of the fin, and it had a brake to stop flutter by significantly increasing the first fin bending mode frequency. The flexibility of the model was limited to the mounting (roll only) and the fin (mainly torsion but also some bending). The first fin bending mode had a frequency of 2.62 Hz and a damping ratio of 0.6%, and the fin torsion mode had a frequency of 4.64 Hz and a damping ratio 2.1%. Compared with the model of Jennings and Berry [8], the present model had a practically rigid HTP, thereby removing the uncertainty of the stabilizer dihedral induced by static load.

The design flutter speed without trim load was 55 m/s equivalent airspeed. The pitch of the HTP could be controlled by an electric actuator inside the fin tip fairing. Excitation for the test was provided by DEI flutter vanes (named after their manufacturer, Dynamic Engineering, Inc.) mounted on the wind-tunnel side walls upstream of the test section (Fig. 6). The instrumentation consisted of a single triaxial accelerometer mounted at midspan in the left stabilizer.

The flutter analysis was performed for the wind-tunnel altitude in the standard atmosphere to obtain a reasonable matching of reduced

Table 1   Comparison of static generalized forces due to yaw for Stark's T-tail [16]

Coefficient	Method	$M = 0.0$	$M = 0.8$
Yawing moment	[16]	−0.0990	−0.1295
	[18]	−0.0970	−0.1242
	Present	−0.0811	−0.1067
Side force	[16]	−0.5173	−0.5947
	[18]	−0.5355	−0.6170
	Present	−0.5409	−0.6181
Rolling moment	[16]	−0.1231	−0.1238
	[18]	−0.1255	−0.1258
	Present	−0.1319	−0.1323

Table 2   Comparison of unsteady generalized forces for Stark's T-tail at $M = 0.8$ and $k = 0.2$ [16]

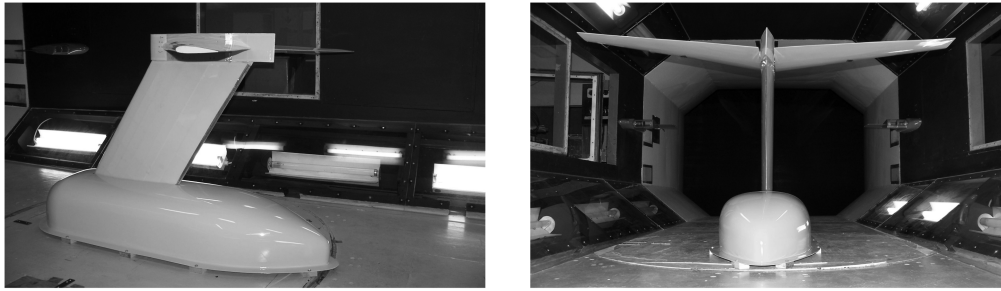| Coefficient | Method | Motion | | | | | |
| | | Yawing | | Sideways | | Rolling | |
		Re	Im	Re	Im	Re	Im
Yawing moment	[19]	−0.0528	−0.4773	0.0456	−0.0228	0.0126	0.0237
	[16]	−0.0961	−0.4811	0.0412	−0.0300	0.0125	0.0239
	[18]	−0.0837	−0.5270	0.0470	−0.0278	0.0137	0.0257
	Present	−0.0733	−0.4971	0.0448	−0.0256	0.0144	0.0263
Side force	[19]	−0.5422	−0.3721	0.0305	−0.1098	0.0166	−0.0270
	[16]	−0.6108	−0.3625	0.0241	−0.1211	0.0158	−0.0295
	[18]	−0.6270	−0.3965	0.0297	−0.1260	0.0171	−0.0318
	Present	−0.6295	−0.3753	0.0270	−0.1252	0.0176	−0.0338
Rolling moment	[19]	−0.1176	−0.1210	0.0149	−0.0249	0.0177	−0.0478
	[16]	−0.1247	−0.1151	0.0134	−0.0255	0.0179	−0.0497
	[18]	−0.1270	−0.1266	0.0154	−0.0269	0.0186	−0.0529
	Present	−0.1345	−0.1306	0.0159	−0.0282	0.0192	−0.0542

Fig. 6   T-tail flutter model installed in wind tunnel.

frequency. A single Mach number of 0.167 was used in the analysis, corresponding to 55 m/s equivalent airspeed. The sensitivity of the analytical results to the paneling density was investigated by using three paneling schemes to predict the flutter and divergence speeds for zero HTP incidence and neglecting the camber of the stabilizers. The divisions were evenly spaced in both spanwise and chordwise directions of all the lifting surfaces. There were 290 source panels on the root fairing in all cases. The wind-tunnel floor was modeled as a symmetry plane, while the tunnel side walls and roof were not modeled. The results in Table 3 indicate that the predicted flutter and divergence speeds are not overly sensitive to the aerodynamic box size. The second paneling scheme was used for the comparison to the wind-tunnel test results, as this scheme is representative of what would be used in practice. This paneling scheme is illustrated in Fig. 7, with the root fairing cut away to reveal the image system of the fin inside the fairing. The image system is explained in [6]. The flutter and divergence speeds predicted by the standard DLM of [6] for the second paneling scheme were 48.88 and 68.32 m/s, respectively. The difference between the predicted flutter speeds from the standard DLM and the enhanced DLM is entirely due to the steady load induced on the HTP by the displacement effect of the root fairing. Without the fairing, but retaining the image system of the fin inside the fairing, both codes predicted flutter and divergence speeds of 48.58 and 68.06 m/s, respectively.

Modeling the camber of the stabilizers mounted upright resulted in an upward trim load and a 2.38 m/s decrease in predicted flutter speed to 47.04 m/s. Conversely, modeling the camber of the stabilizers mounted upside down resulted in a downward trim load and an increase of 2.82 m/s in predicted flutter speed to 52.24 m/s. For the analyses including the airfoil camber and pitch deflection, the pitch deflection of the HTP was added to the camber definition in the geometry input. The quadratic mode shape components of the individual modes were estimated by dividing the model into finite-element-like plate elements and calculating the in-plane deformation of each element required to minimize the in-plane stretching that is proportional to the square of the linear modal displacements (cf. Eq. 22 of [13]).

The flutter analysis indicated both a flutter instability and divergence. The predicted divergence speed was above the flutter speed, except for large downward trim loads, i.e., for the stabilizers mounted upside down and pitched four or more degrees down. The predicted flutter speed decreased significantly for upward trim loads and increased even more sharply for downward trim loads. The effect of neglecting the quadratic mode shape components was investigated by repeating the calculations with the quadratic mode shape components set equal to zero.

The wind-tunnel tests were conducted in the Council for Scientific and Industrial Research's low-speed closed-circuit wind tunnel, which has a nominal test section size of 2.134 × 1.524 m (7 × 5 ft)

and a speed range of up to 100 m/s. The tunnel is located in Pretoria, South Africa, approximately 1340 m (4400 ft) above sea level. The test section is vented to ambient pressure. Speed control was based on dynamic pressure, calculated to match the nominal equivalent airspeed of each test point.

Two test series were conducted. In the first series, a range of HTP incidence angles, with the stabilizers alternately mounted upright and upside down, was tested to obtain the general trend of flutter speed with trim load without exceeding the design flutter speed of 55 m/s. A second test series was conducted specifically to verify the predicted sharp increase in flutter speed with downward static load. For the latter test series, the stabilizers were only mounted upside down, i.e., cambered to produce a downward static load.

For each HTP setting, the flutter speed was determined as follows:

1) With the tunnel speed stabilized, the brake was released, and it was observed whether the model fluttered without excitation.

2) If the model did not flutter, excitation was applied in the form of a fast antisymmetric sweep of the DEI flutter vanes, from zero to 16 Hz.

3) If the model fluttered with excitation, the brake was applied to stop the flutter. The speed was then increased in steps of 1 m/s until the model fluttered without excitation.

4) If the model did not flutter with excitation, the speed was increased by 1 m/s, and the procedure repeated.

The measured flutter speeds from the first test series are compared with the predicted values in Fig. 8. The flutter speed range shown for the measured values is from the highest speed at which the model did not flutter with excitation to the lowest speed at which the model fluttered without excitation. Both the flutter speed and the flutter speed trend with HTP incidence were reasonably well predicted. The flutter speed predicted using the standard DLM, which does not have a means of incorporating the effect of the trim load, is also shown.

Flutter and divergence speeds for the stabilizer mounted upside down (i.e., cambered for generating downward lift), calculated using only the linear mode shape components and using parabolic mode shapes, are compared with results from the second test series in Fig. 9. Omitting the quadratic mode shape components in the enhanced DLM is, in principal, similar to the method of Suciu [9]. In this case, the quadratic mode shape components had little effect on the predicted flutter speeds, but they had a significant effect on the predicted divergence speed. With the quadratic mode shape components included, the divergence speed is predicted to decrease slightly with increasing downward lift. With the quadratic mode shape components omitted, the divergence speed is predicted to increase significantly with increasing downward lift. This discrepancy is in agreement with the inference from the rolling T-tail example.

In the wind-tunnel test, with the stabilizers mounted upside down and pitched 2 deg down, the model did not flutter with or without excitation at 60 m/s. At 61 m/s, the model was destroyed due to

Table 3   Flutter and divergence speed dependence on paneling (span × chord)

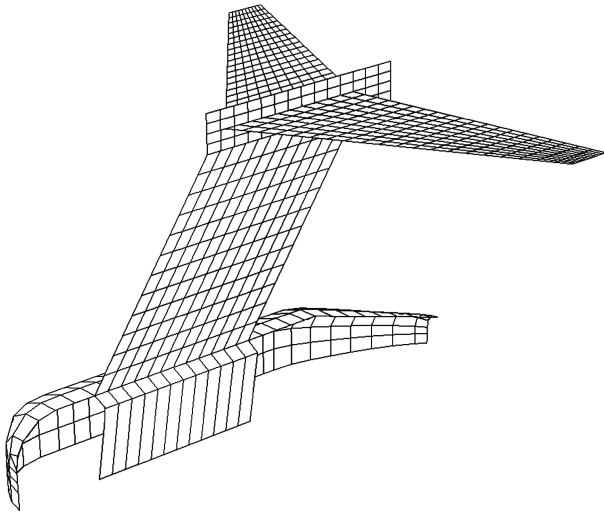| Scheme	Fin	Fin tip fairing	Stabilizers	Total boxes	Flutter speed, m/s	Divergence speed, m/s
1	6 × 6	2 × 7	10 × 5	440	49.42	67.67
2	12 × 12	4 × 14	20 × 10	890	49.42	67.74
3	24 × 24	8 × 28	40 × 20	2690	49.45	67.82

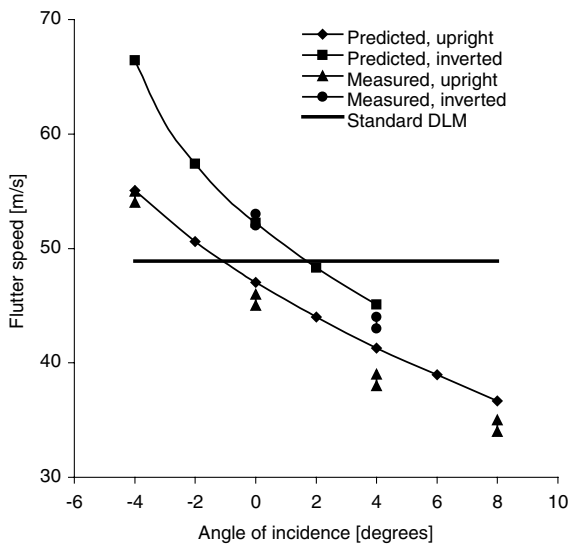**Fig. 7   Aerodynamic model of T-tail flutter model.**

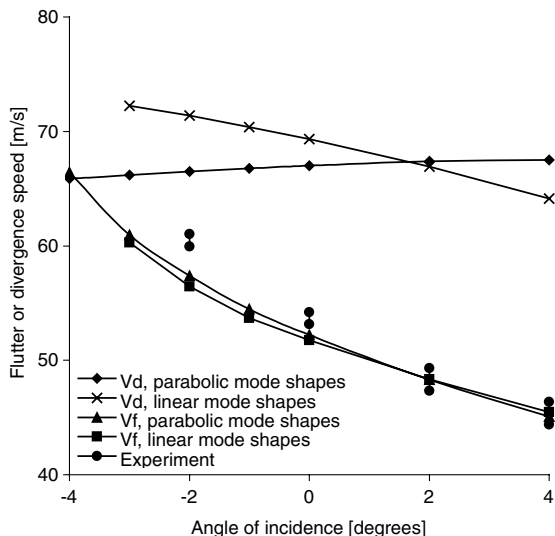**Fig. 8   T-tail model flutter speed vs HTP incidence.**

Fig. 9   Flutter and divergence speed, with and without quadratic mode shape components.

static divergence. Although the flutter speed was significantly underpredicted and the divergence speed significantly overpredicted, the result at least confirmed the sharp increase in flutter speed with downward trim load and that the predicted divergence speed, taking quadratic mode shape components into account, was closer to the experimental result than the divergence speed predicted using linear mode shapes.

Conclusions

The enhanced DLM calculates all the unsteady air loads that are necessary to predict T-tail flutter. This was achieved by using the generalized boundary condition of the wing–body DLM described in [6], as well as generalizing the calculation of forces. In addition, the steady-state loads and the quadratic mode shape components are taken into account in the calculation of generalized aerodynamic forces.

In cases without steady aerodynamic loads (i.e., trim loads), the enhanced DLM produces identical results to the standard DLM of [6]. However, the standard DLM has no means for calculating the effect of steady loads on the flutter characteristics of T-tails, which is known to be significant. It is therefore common practice to calculate additional aerodynamic coefficients outside of the DLM and add them to the DLM results to account for the effect of trim loads: the method of Suciu being one possible procedure [9].

When airfoil camber, steady angle of attack, and control deflections are specified, the enhanced DLM produces results similar to the method of Suciu [9], without the need for calculating additional aerodynamic coefficients outside of the DLM. In addition, if quadratic mode shape components are specified, an inconsistency in the method of Suciu, related to the rotation of the steady loads, is eliminated.

Comparisons with experimental results for a T-tail flutter model showed that the enhanced DLM accurately predicted the effect of trim load on flutter speed. The effect of including the quadratic mode shape components on the predicted flutter speed of the model was small, but the effect on the predicted divergence speed was significant.

Acknowledgments

References

[1] Rodden, W. P., "The Development of the Doublet-Lattice Method," *Proceedings of the International Forum on Aeroelasticity and Structural Dynamics*, Vol. 2, Assoc. Italiana di Aeronautica et Astronautica, Rome, June 1997, pp. 1–7.

[2] Albano, E., and Rodden, W. P., "A Doublet-Lattice Method for Calculating Lift Distributions on Oscillating Surfaces in Subsonic Flows," *AIAA Journal*, Vol. 7, No. 2, Feb. 1969, pp. 279–285.
doi:10.2514/3.5086

[3] Albano, E., and Rodden, W. P., "Errata: 'A Doublet-Lattice Method for Calculating Lift Distributions on Oscillating Surfaces in Subsonic Flows'," *AIAA Journal*, Vol. 7, No. 11, Nov. 1969, p. 2192.
doi:10.2514/3.55530

[4] Rodden, W. P., Giesing, J. P., and Kalman, T. P., "Refinement of the Nonplanar Aspects of the Subsonic Doublet-Lattice Lifting Surface Method," *Journal of Aircraft*, Vol. 9, No. 1, Jan. 1972, pp. 69–73.
doi:10.2514/3.44322

[5] Rodden, W. P., Taylor, P. F., and McIntosh, S. C., Jr., "Further Refinement of the Nonplanar Aspects of the Doublet-Lattice Method," *Journal of Aircraft*, Vol. 35, No. 5, 1998, pp. 720–727.
doi:10.2514/2.2382

[6] Van Zyl, L. H., "Unsteady Panel Method for Complex Configurations Including Wake Modeling," *Journal of Aircraft*, Vol. 45, No. 1, Jan.–Feb. 2008, pp. 276–285.
doi:10.2514/1.29267

[7] Queijo, M. J., "Theory for Computing Span Loads and Stability Derivatives Due to Sideslip, Yawing, and Rolling for Wings in Subsonic Compressible Flow," NASA TN D-4929, Dec. 1968.

[8] Jennings, W. P., and Berry, M. A., "Effect of Stabilizer Dihedral and Static Lift on T-Tail Flutter," *Journal of Aircraft*, Vol. 14, No. 4, April 1977, pp. 364–367.
doi:10.2514/3.58785

[9] Suciu, E., "MSC/NASTRAN Flutter Analysis of T-Tails Including Horizontal Stabilizer Static Lift Effects and T-Tail Transonic Dip," *MSC 1996 World User's Conference Proceedings*, MSC Software Corp., Santa Ana, CA, June 1996, pp. 1–10.

[10] Kalman, T. P., Giesing, J. P., and Rodden, W. P., "Spanwise Distribution of Induced Drag in Subsonic Flow by the Vortex Lattice Method," *Journal of Aircraft*, Vol. 7, No. 6, Nov.–Dec. 1970, pp. 574–576.
doi:10.2514/3.44219

[11] Hancock, G. J., "Comment on 'Spanwise Distribution of Induced Drag in Subsonic Flow by the Vortex Lattice Method'," *Journal of Aircraft*, Vol. 8, No. 8, Aug. 1971, pp. 681–682.
doi:10.2514/3.44294

[12] Kalman, T. P., Giesing, J. P., and Rodden, W. P., "Reply by Authors to G. J. Hancock," *Journal of Aircraft*, Vol. 8, No. 8, Aug. 1971, pp. 681–682.

[13] Dohrmann, C. R., and Segalman, D. J., "Use of Quadratic Components for Buckling Calculations," Sandia National Labs., SAND-96-2367C, Albuquerque, NM, 1996.

[14] Robinett, R. D., III, Wilson, D. G., Eisler, G. R., and Hurtado, J. E., "Applied Case Studies," *Applied Dynamic Programming for Optimization of Dynamical Systems*, Soc. for Industrial and Applied Mathematics, Philadelphia, 2005, pp. 134–150.

[15] Jung, K. J., Lee, J., Kwon, J. H., and Kang, I., "The Quadratic Mode Method for Fluid-Structure Coupling of High Aspect Ratio Wing," AIAA Paper 2008-5864, Sept. 2008.

[16] Stark, V. J. E., "Aerodynamic Forces on a Combination of a Wing and a Fin Oscillating in Subsonic Flow," SAAB Aircraft Co., TN-54, Linkoping, Sweden, 1964.

[17] Rodden, W. P., "Comment on 'Effect of Stabilizer Dihedral and Static Lift on T-Tail Flutter'," *Journal of Aircraft*, Vol. 15, No. 7, July 1978, pp. 447–448.
doi:10.2514/3.58387

[18] Kalman, T. P., Rodden, W. P., and Giesing, J. P., "Application of the Doublet-Lattice Method to Nonplanar Configurations in Subsonic Flow," *Journal of Aircraft*, Vol. 8, No. 6, June 1971, pp. 406–413.
doi:10.2514/3.59117

[19] Dusto, A. R., and Epton, M. A., "An Advanced Panel Method for Analysis of Arbitrary Configurations in Unsteady Subsonic Flow," NASA CR 152323, Feb. 1980.